RSC Advances

PAPER

View Article Online
View Journal | View Issue

Cite this: *RSC Adv.*, 2025, **15**, 3339

Preparation and structural optimization of vanadium oxide nanotubes as cathode materials for PIBs with improved performance†

Yuan Xie,[a] Jia Wen,[a] Junyuan Huang,[a] Rong Jiang,[a] Longjun Dai,[a] Yang Ren,[a] Zhu Liu[ab] and Xiaowei Zhou *[a]

Received 27th October 2024
Accepted 19th January 2025

DOI: 10.1039/d4ra07672a

rsc.li/rsc-advances

In this work, we synthesized hollow multi-walled vanadium oxide nanotubes (VO_x-NT) using a soft template technique under hydrothermal reaction conditions. By replacing organic templates, which do not contribute to electrochemical potassium storage, with K^+ in a solution environment, we effectively retained the original hollow multi-walled structure of VO_x-NT while obtaining the K-VO_x-NT material. We conducted systematic characterizations of the microstructure, morphology, and composition of these materials and evaluated their potassium storage performance. Compared to the original VO_x-NT, K-VO_x-NT exhibited significantly enhanced cycling stability and rate performance when serving as the cathode in potassium-ion batteries (PIBs). It demonstrated a reversible discharge specific capacity of 75.7 mA h g^{-1} for the 1st cycle at a current density of 50 mA g^{-1} within a voltage range of 1.5–3.8 V (*vs.* K^+/K) and retained 62.2 mA h g^{-1} after the 50th cycle. When a current density of 600 mA g^{-1} was applied, it could still deliver a capacity of 44.3 mA h g^{-1}. Furthermore, the storage and degradation mechanisms of K^+ in K-VO_x-NT were elucidated. In addition, using hard carbon as the anode, the K-VO_x-NT full-cell was tested to further evaluate its practical performance. This work provides insight into the design and modification of vanadium-based cathode materials for future PIBs.

1. Introduction

Nowadays, effective energy storage is a crucial aspect of industrial production and daily life. In recent decades, lithium-ion batteries (LIBs) have dominated the energy storage market owing to their high energy and power density.[1–3] However, in view of the high cost and limited shortage of lithium resources as well as the need for sustainable development in large-scale energy storage for the future, there is an urgent need to explore new alternatives and supplements for LIBs.[4,5] Notably, K^+ exhibits chemical properties similar to those of Li^+ and Na^+ but with a smaller Stokes radius in the electrolyte than both, which could facilitate its ionic conductivity in the electrolyte.[6,7] Moreover, K^+ possesses a lower standard potential (−2.93 V *vs.* SHE) than Na^+ (−2.71 V *vs.* SHE), which is closer to that of Li^+ (−3.04 V *vs.* SHE).[8,9] Thus, potassium-ion batteries (PIBs) can be considered promising candidates for future electrochemical energy storage devices with relatively high working voltage and energy density.[5–10] At present, significant progress has been made in research on anode materials for PIBs, with a strong focus on carbon-based materials and their nanocomposites, such as various amorphous carbons, metal/C (Sb/C, Sn/C, *etc.*) and metal chalcogenide/carbon nanocomposites (Bi_2S_3/C, Sb_2Se_3/C, *etc.*).[11,12] Generally, these materials deliver high capacity for potassium storage and display great potential for practical applications. However, advancements in cathode materials remain unsatisfactory, limiting the overall performance and future commercialization of PIBs.[13,14]

In order to develop PIBs with high performance, it is crucial to investigate cost-effective cathodes with optimal electrochemical performance. The most studied cathode materials for PIBs are Prussian blue (PB) and its analogs (PBAs), whose unique three-dimensional channel structures can provide abundant active sites for K^+.[15,16] However, PB and PBAs suffer from some inherent drawbacks, such as poor conductivity, thermal stability and the presence of interstitial water, which can impact their K^+ storage properties.[17] Another type of transition metal oxide (TMO) (M = Mn, Co, Cr, V, *etc.*) has attracted the attention of researchers due to its easy preparation in air, stability and special layered structure, which could provide smooth pathways for fast transport and effective storage of K^+.[18,19] Among these TMOs, a typical representative is vanadium oxide, which has the advantages of facile synthesis and an inherent multi-channel framework, facilitating the rapid diffusion of K^+.[20] According to previous reports, Deng *et al.* prepared

[a]*Department of Physics, School of Physics and Astronomy, Yunnan University, Kunming, Yunnan, 650504, China. E-mail: zhouxiaowei@ynu.edu.cn*

[b]*Yunnan Key Laboratory of Micro/Nano-Materials and Technology, School of Materials and Energy, Yunnan University, Kunming, 650504, China*

† Electronic supplementary information (ESI) available. See DOI: https://doi.org/10.1039/d4ra07672a

a kind of $K_{0.5}V_2O_5$ nanobelt by hydrothermal reaction with K^+ pre-intercalated into layered V_2O_5, which exhibited an initial capacity of 60 mA h g^{-1} under 100 mA g^{-1} between 1.5 and 3.8 V and retained 51.6 mA h g^{-1} after 100 cycles.[21] Xu *et al.* reported NH_4^+ inserted $NH_4V_4O_{10}$ with a flower-like architecture, which was synthesized *via* hydrothermal reaction utilizing V_2O_5 as the vanadium source and NH_4Cl as the ammonium source. It delivered a relatively high capacity of 80 mA h g^{-1} at 50 mA g^{-1} for the 2nd discharge within a voltage range of 2–3.8 V and retained a value of 75 mA h g^{-1} after 200 cycles, indicating good cycling stability.[22] Evidently, it is an effective strategy to adjust the interlayer spacing of vanadium oxide for enhancing K^+ storage.

In particular, vanadium oxide nanotubes (VO_x-NT) with a hollow and multi-walled microstructure were successfully fabricated under hydrothermal conditions using V_2O_5 as the precursor and suitable organic amines with long-chains as the soft template.[23] Typically, Nordlinder *et al.* have applied this VO_x-NT as the cathode material for lithium-ion batteries (LIBs), which exhibited a large capacity of up to 250 mA h g^{-1} for the 2nd discharge.[24] The unique microstructure of VO_x-NT can offer plentiful active sites, which is beneficial for the storage of Li^+. It is expected that VO_x-NT can also provide similar advantages for K^+ storage. Therefore, it is necessary and meaningful to explore the potential of VO_x-NT as the cathode for PIBs. In this study, VO_x-NT was synthesized through a one-step hydrothermal process adopting V_2O_5 as the vanadium source and dodecylamine ($C_{12}H_{27}N$) as the soft template. In addition, the K^+-exchange technique was performed and the organic template within VO_x layers was effectively removed, resulting in the generation of K-VO_x-NT. We conducted a comprehensive analysis and comparison between VO_x-NT and K-VO_x-NT by various characterization methods and electrochemical K^+ storage tests. The relationship between their reversible electrochemical K^+ storage performances, mechanisms and microstructures was systematically discussed and elucidated. We presented the intrinsic reasons and mechanism for the degradation of reversible K^+ storage performance in VO_x-NT. A feasible strategy to enhance the K^+ storage properties of VO_x-NT *via* the cation-exchange method was proposed. This research provides valuable insights to design vanadium-based cathode materials with high-performance for PIBs through interlayer microstructure regulation.

2. Experimental section

2.1 Preparation of VO_x-NT and K-VO_x-NT

Specifically, 0.91 g of V_2O_5 powder was dispersed in 70 mL of deionized (DI) water and stirred for 30 min. Next, 0.93 g of dodecylamine ($C_{12}H_{27}N$) was dissolved in 3 mL of ethanol. Then, this solution was added to the above V_2O_5 dispersion and stirred continuously for another 12 h to form a uniform yellow suspension. Subsequently, the suspension was transferred to a 100 mL Teflon-lined autoclave and sealed, which was subjected to hydrothermal treatment in an oven at 180 °C for 5 days. Finally, a black product was obtained *via* centrifugation, washing and drying, which was denoted as VO_x-NT.

For the preparation of K^+-exchanged VO_x-NT (K-VO_x-NT), firstly, 0.4 g of as-prepared VO_x-NT was dispersed in a mixed solution containing 80 mL of anhydrous ethanol and 20 mL of DI water with agitation for 30 min. Then, 8 g of KCl was dissolved into the above black suspension, which was stirred continuously for 12 h to conduct the K^+ exchange process. The resulting product was washed, dried and labeled as K-VO_x-NT.

2.2 Characterization

X-Ray Diffraction (XRD, TTRIII-18KW, Rigaku) was employed to study the crystalline structure of samples over a 2θ angle range from 2° to 60° using Cu Kα (λ = 1.5406 Å) radiation. Field emission scanning electron microscopy (FESEM, Nova Nano 450, FEI) and transmission electron microscopy (TEM, JEOL, JEM-F200) were utilized to observe the morphology and microstructure of target samples. TEM was equipped with high angle annular dark field (HAADF) imaging and energy dispersive X-ray spectroscopy (EDS). Raman spectra were collected by using a spectrometer (Renishaw inVia, λ = 514.5 nm) in the wave-number range of 100 to 1800 cm^{-1}. Fourier transform infrared (FTIR) spectra were recorded through a spectrometer (BFRL, WQF-520A) in the wave-number range from 400 to 4000 cm^{-1} based on KBr tabletting. Thermogravimetric analysis-differential scanning calorimetry (TGA/DSC1/1600LF, Mettler Toledo) was performed in air environment with a heating rate of 10 °C min^{-1}. X-ray photoelectron spectroscopy (XPS, K-Alpha, Thermo Scientific) was carried out to determine the elemental components and valence information of samples.

2.3 Electrochemical measurement

The cathode was fabricated by mixing the active material (VO_x-NT or K-VO_x-NT), a conductive agent (carbon black) and a binder (polyvinylidene fluoride, PVDF) with a mass ratio of 7 : 2 : 1 using *N*-methyl-2-pyrrolidone (NMP) as the solvent. The slurry formed was uniformly coated on Al foil and heated at 100 °C for 10 h under vacuum. Then, the cathode plate dried was cut into a circular wafer with a diameter of 8 mm, which was used as the working electrode. For galvanostatic charge–discharge (GCD) tests, the active mass of VO_x-NT or K-VO_x-NT on the working electrode was approximately 1.7 mg cm^{-2}. The CR2025 coin-cell was assembled in an argon-filled glove box with both moisture and oxygen concentrations below 0.01 ppm. A porous glass fiber membrane (GF/D) was utilized as the separator and K metal as both counter and reference electrodes. The electrolyte consisted of 1 M potassium bis(fluorosulfonyl) imide (KFSI), which was dissolved in a mixed solvent of ethyl carbonate (EC) and diethyl carbonate (DEC) with a 1 : 1 volume ratio. An electrochemical workstation (CHI660) was utilized to conduct cyclic voltammetry (CV) within the voltage range of 1.5–3.8 V (*vs.* K/K^+) under various scan rates. A LAND battery test system (CT2001A) was employed to measure the GCD performance of cathodes at different current densities between 1.5 and 3.8 V. The CHI660 was also adopted to perform electrochemical impedance spectroscopy (EIS) in a frequency range from 100 kHz to 0.01 Hz by applying an alternating current (AC) signal with an amplitude of 5 mV. The galvanostatic

intermittent titration technique (GITT) was performed on a CT2001A through alternate application of pulse current (lasting 15 min with a current density of 20 mA g^{-1}) and relaxation process (lasting 45 min in an open circuit state). All electrochemical tests were carried out under ambient temperature. To evaluate the practical performance of the K-VO_x-NT cathode in a full-cell, we employed hard carbon (Kuraray, Type 1) as the standardized anode, which was slightly excessive when matched with K-VO_x-NT (N/P ratio: ~1.1). This hard carbon anode was pre-intercalated with K^+. The GCD tests of the hard carbon half-cell were conducted in the voltage range of 0.01–2.5 V under 50 mA g^{-1}. The GCD tests of the full-cell were performed in the voltage range of 1.0–3.6 V under 50 mA g^{-1}. The rate capability of the full-cell was evaluated within the same voltage range with different N/P ratios of ~1.1 and 4.0 (refer to the ESI†).

3 Results and discussion

The cross-sectional microstructures of VO_x-NT and K-VO_x-NT are presented in Fig. 1(a), which can be depicted as rolled or concentric vanadate layers (VO_x) intercalated by protonated dodecylamine ($C_{12}H_{25}NH_3^+$). In the hydrothermal reaction, $C_{12}H_{27}N$ served as a soft template and at the same time a weak reducing agent, guiding the formation of VO_x-NT by a curl formation mechanism. During the hydrothermal reaction that forms VO_x-NT, the organic template ($C_{12}H_{25}NH_3^+$), which is located between the VO_x layers, acts as a reducing agent. The reduction induces a partial conversion of V^{5+} to V^{4+} within the VO_x layers, which consequently leads to the changes of internal stress in VO_x layers. As a result, the VO_x layers undergo directional curling, ultimately forming a multilayered tubular structure (VO_x-NT).[25–27]

With regard to the VO_x layer, it resembles the triclinic crystal system of $BaV_7O_{16}\cdot nH_2O$ bronze.[23,25] $C_{12}H_{25}NH_3^+$ between VO_x layers would be effectively removed by the K^+ exchange process, resulting in an obvious reduction of distance between VO_x layers. Simultaneously, K^+ will enter the interlayer of VO_x layers to maintain the overall electrical neutrality of VO_x-NT, finally forming K-VO_x-NT. It is worth noting that throughout this process, the two-dimensional microstructure of VO_x layers is well preserved. XRD patterns and relevant fittings for the two samples are shown in Fig. 1(b), which reveal two series of diffraction peaks: (00l) series, which is in the small-angle region (2°–15°), reflects the periodic layered structure of VO_x-NT and directly indicates the spacing of VO_x layers *via* the corresponding calculation, and (*hk*0) series, which is in the large-angle region (15°–50°), demonstrates the microstructural features of the two-dimensional VO_x layer itself.[27] It can be observed that after K^+ exchange, the diffraction peaks of K-VO_x-NT are noticeably broader compared to those of VO_x-NT, indicating an increase in its amorphous nature. The peak positions of the (*hk*0) series in the large angle region don't display obvious shifting, indicating that the K^+ exchange process has hardly affected the microstructure of 2D VO_x layers. The (00l) peak in the small-angle region shifts from 3.22° for VO_x-NT to 9.5° for K-VO_x-NT through K^+ exchange. According to Bragg's law, it

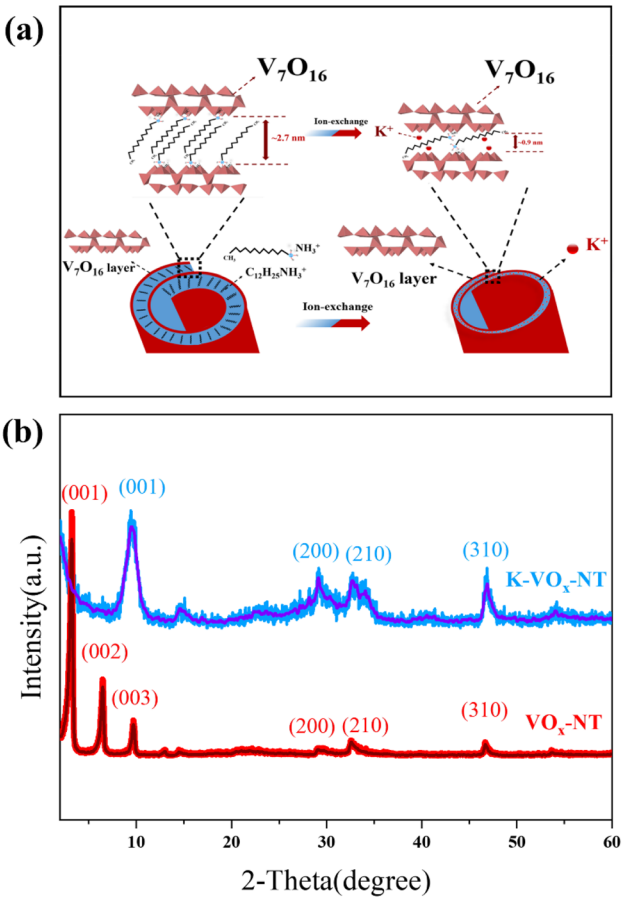

Fig. 1 (a) Schematic of the microstructure of VO_x-NT and illustration of the K^+ exchange process; (b) XRD patterns and relevant fittings of VO_x-NT and K-VO_x-NT.

indicates that the interlayer spacing of VO_x-NT decreases from ~2.74 nm to ~0.93 nm. It is because $C_{12}H_{25}NH_3^+$ with a long chain-length between VO_x layers is replaced by K^+ with a relatively small diameter, reducing the interlayer distance.

TEM and HR-TEM images of VO_x-NT (a–c) and K-VO_x-NT (d–f) are given in Fig. 2. It can be seen that both samples are hollow and multi-walled nanotubes. The dark lattice fringes represent VO_x layers and the bright stripes correspond to the protonated dodecylamine template. The difference is that the interlayer distance between VO_x layers for K-VO_x-NT in Fig. 2(f) decreases from ~2.7 nm for VO_x-NT in Fig. 2(c) to ~0.9 nm. This change corresponds well with XRD results and the K^+ exchange mechanism proposed. It indicates that the protonated dodecylamine between the VO_x layers of VO_x-NT was effectively removed *via* K^+ exchange. EDX mapping in Fig. 2(g) shows that K, N, O, V and C elements are evenly distributed in K-VO_x-NT, which illustrates that K^+ enters the interlayer of VO_x layers successfully after the exchange process and there is still a small amount of residual dodecylamine in K-VO_x-NT, as evidenced by the FTIR spectrum in Fig. S1† and the TGA-DSC test in Fig. 4(d). It should be noted that the clarity of C element in EDX mapping is due to the fact that K-VO_x-NT was tested on a carbon-coated copper mesh. Therefore, it is difficult to avoid the interference from inherent

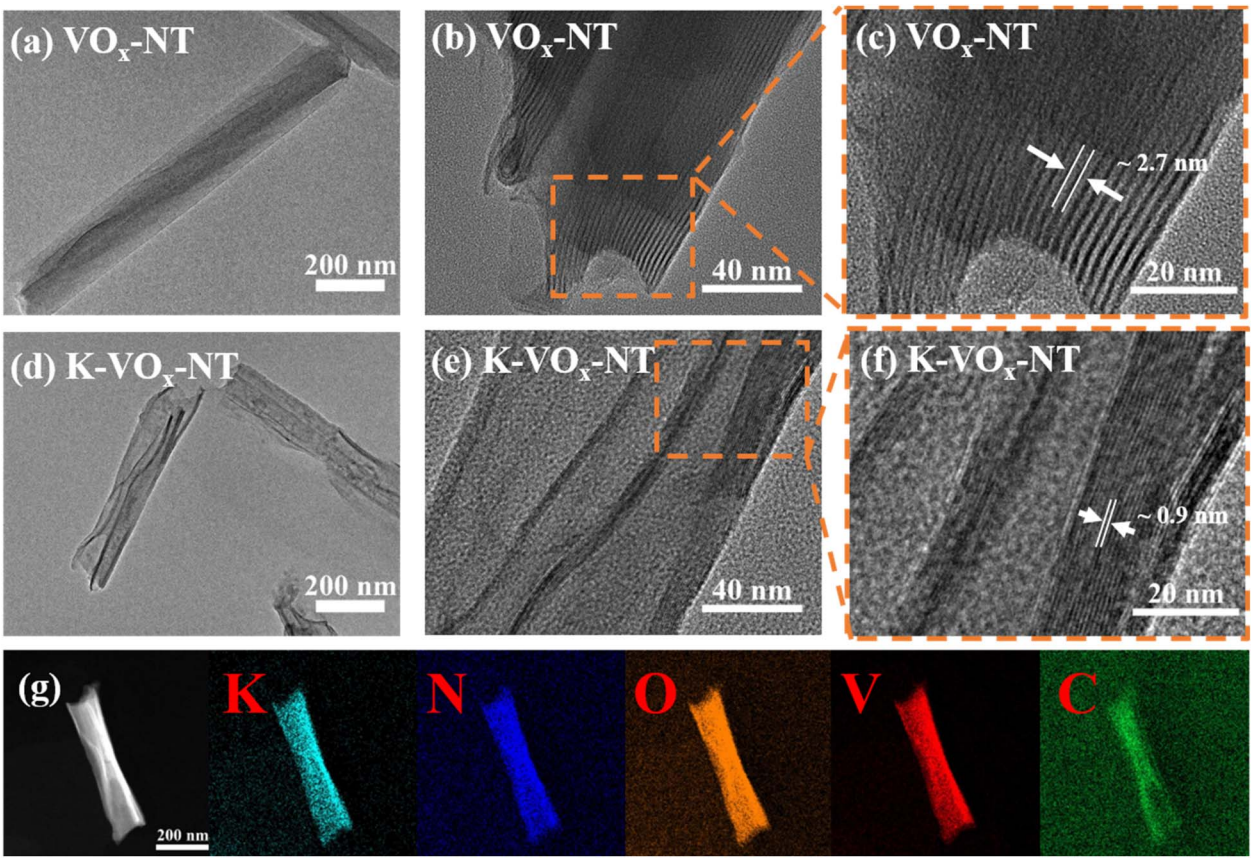

Fig. 2 TEM and HR-TEM images of VO_x-NT (a–c) and K-VO_x-NT (d–f); HAADF image and the corresponding elemental mappings for K-VO_x-NT (g).

carbon on carbon-coated copper mesh. Besides, EDX mapping is also sensitive to carbon element that still exists in residual organic dodecylamine. However, the original hollow and multi-walled microstructure of VO_x-NT has been maintained.

Fig. 3 shows the SEM images of VO_x-NT (a, b) and K-VO_x-NT (c, d). It clearly demonstrates that both samples possess a hollow tubular morphology and internal curling feature, especially as observed in Fig. 3(d). This phenomenon is consistent with the aforementioned TEM observations. The diameter and length for both samples are ~100–200 nm and ~2–5 μm, respectively. It is worth mentioning that the tube wall of K-VO_x-NT has become thinner and its diameter becomes larger compared to VO_x-NT, which may be caused by stress release when the curly structure relaxes during K^+ exchange. TEM observations corroborate again the curl formation mechanism proposed earlier.

FTIR spectra for the two samples are depicted in Fig. 4(a), where the absorption peaks at ~485 and ~574 cm^{-1} correspond to V–O–V symmetric stretching and deforming vibrations of the vanadium oxygen polyhedron.[14,28] The peak at ~1001 cm^{-1} can be attributed to the V=O asymmetric stretching mode. The positions of these peaks, which could be designated as vibration modes of vanadium–oxygen bonds, have hardly shifted before and after K^+ exchange. This illustrates that the microstructure of VO_x layers in VO_x-NT is basically not affected by K^+ exchange. The absorption peaks at ~1611 and 3400 cm^{-1} for both samples are caused by bending and stretching vibrations of O–H bonds in surface adsorbed and deep crystalline water, respectively.[14,29,30] Due to K^+ exchange, the peaks located at ~1461, 2854 and 2919 cm^{-1} for K-VO_x-NT, which can be ascribed to different stretching and bending vibration modes of C–H bonds in dodecylamine, significantly weaken compared with VO_x-NT. Furthermore, the peak at ~3160 cm^{-1}, which can be assigned to the vibration mode of the N–H bond in dodecylamine,[22,28,31] nearly disappears for K-VO_x-NT. These changes suggest that most of the $C_{12}H_{25}NH_3^+$ within VO_x-NT has been removed after K^+ exchange. Raman spectra of the two samples are presented in Fig. 4(b). For K-VO_x-NT, the characteristic peaks at ~164 and 683 cm^{-1} can be assigned to the bending and stretching vibrations of the V–O bond, respectively. The peaks centered at ~265 and 1010 cm^{-1} can be ascribed to the bending and stretching vibrations of the V=O bond. Besides, the peak at ~501 cm^{-1} could be attributed to the stretching mode of the V–O–V bond.[22,32,33] With respect to VO_x-NT, it only exhibits two broadened peaks at ~1390 and 1580 cm^{-1}, which can be attributed to the vibration modes of C–H bonds in dodecylamine, indicating a substantial presence of $C_{12}H_{25}NH_3^+$ in VO_x-NT.[34] However, other characteristic peaks derived from vanadium–oxygen bond vibrations are not distinctly observed for VO_x-NT. It is mainly because the relatively strong vibration

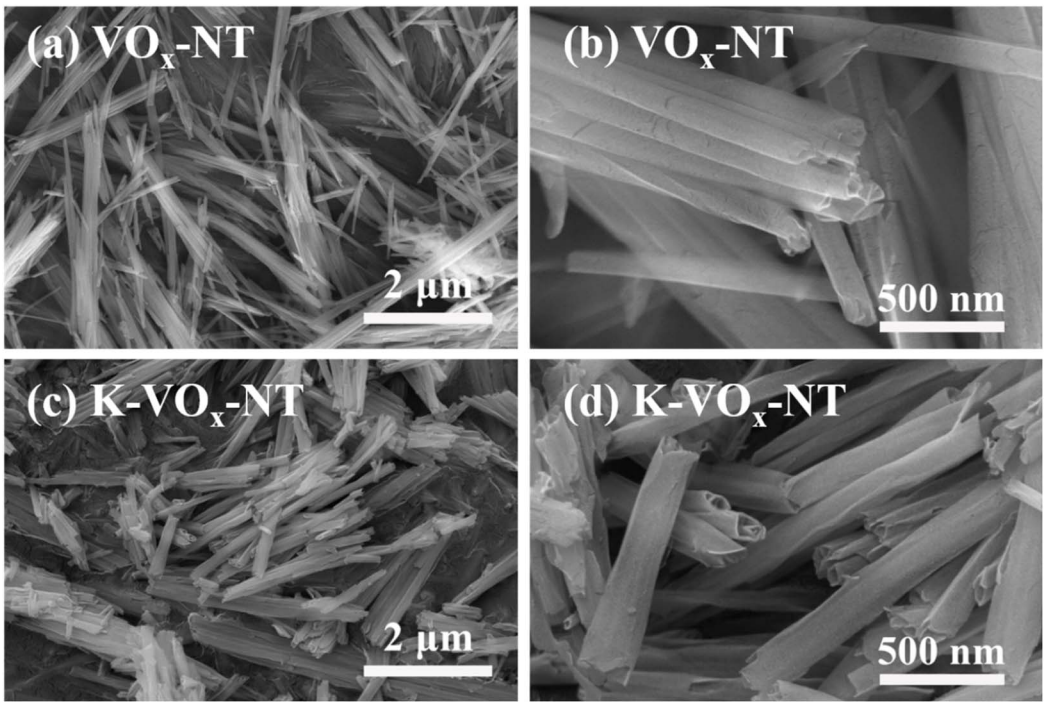

Fig. 3 SEM images of VO_x-NT (a, b) and K-VO_x-NT (c, d) under different magnifications.

modes of C–H bonds in dodecylamine cover the features of vanadium–oxygen bond vibration. Almost no characteristic peaks originating from C–H bond vibration were detected in K-VO_x-NT, suggesting a sufficient exchange of $C_{12}H_{25}NH_3^+$ in VO_x-NT by K^+.

TGA-DSC analyses of VO_x-NT (c) and K-VO_x-NT (d) are illustrated in Fig. 4. For VO_x-NT, a weight loss of ~1.26% from room temperature to 200 °C happens, which is due to the evaporation of adsorbed water and a small quantity of dodecylamine on the surface of VO_x-NT. There is a significant weight loss of ~33.89%

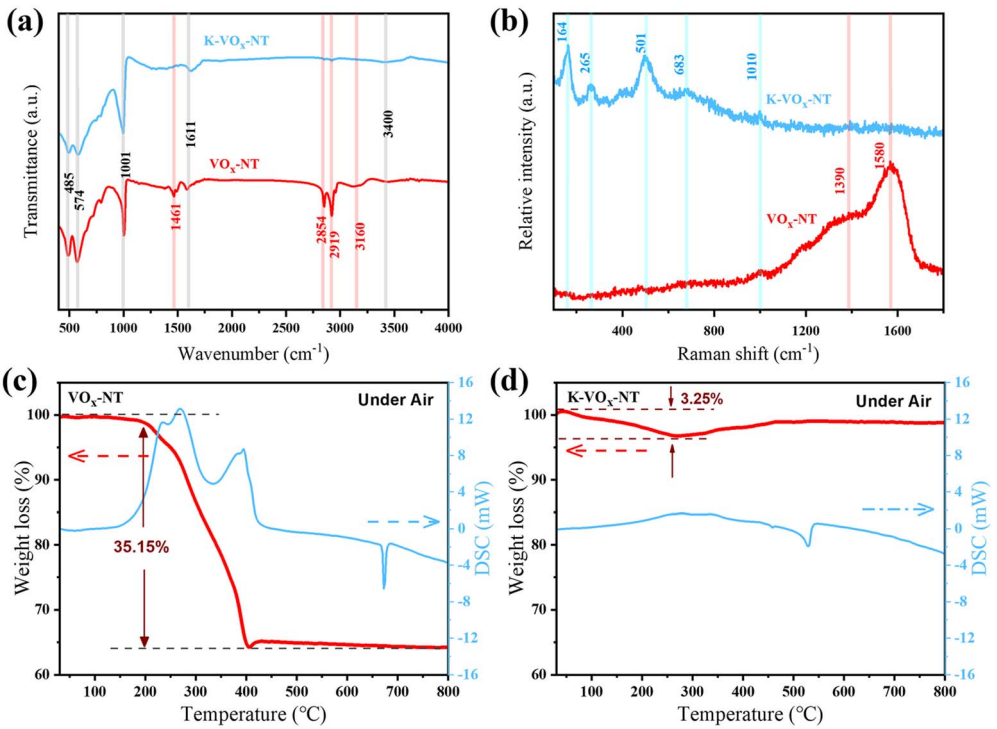

Fig. 4 FTIR (a) and Raman (b) spectra of VO_x-NT and K-VO_x-NT; TGA-DSC curves of VO_x-NT (c) and K-VO_x-NT (d) under air condition.

between 200 and 400 °C, which is primarily brought about by oxidative decomposition of dodecylamine intercalated in VO_x layers. It should be noted that the remaining vanadium oxide will undergo oxidation and recrystallization at the same time. So, weight loss and gain occur simultaneously, but weight loss dominates within this temperature range. The DSC curve for VO_x-NT displays two exothermic peaks: the first one at ~269 °C is mainly due to the oxidative decomposition of dodecylamine; the second one at ~389 °C is jointly caused by the decomposition of dodecylamine and oxidation of residual VO_x. Above 400 °C, a slight increase in weight occurs, which may be owing to the complete oxidation of VO_x (containing a certain amount of V^{4+}) into V_2O_5.[14] A downward endothermic peak at ~673 °C is due to the melting of V_2O_5. In regard to K-VO_x-NT, there is a weight loss of ~3.22% from room temperature to 272 °C, which is mainly caused by the evaporation of adsorbed water and decomposition of residual dodecylamine, whereas a weight gain of ~2.19% happens between ~272 and 480 °C, which is chiefly due to further oxidation of residual K_yVO_x into potassium vanadate with higher V valence. A weak but wide exothermic peak in the temperature range of ~150 to 450 °C can be observed. It can be ascribed to the oxidative reaction of K-VO_x-NT. Similarly, a downward endothermic peak at ~526 °C occurs, which is owing to the melting of remanent potassium vanadate.

General XPS spectra of the two samples are shown in Fig. 5(a) and (c). Compared to VO_x-NT, the relative intensity of the C1s peak for K-VO_x-NT is significantly reduced and its N1s peak has disappeared. Besides, K2s and K2p peaks are detected in K-VO_x-NT. Fig. S2† displays the K2p fine survey spectrum of K-VO_x-NT. Both C1s and N1s mainly originate from dodecylamine, so it indicates that K^+ has effectively replaced the protonated dodecylamine in VO_x-NT to form K-VO_x-NT. Fig. 5(b) and (d) display the V2p fine survey spectra of the two samples, which are characterized by $V2p_{1/2}$ centered at ~524.0 eV and $V2p_{3/2}$ at ~516.6 eV. Both $V2p_{1/2}$ and $V2p_{3/2}$ can be fitted with two peaks, which represent the existence of V^{4+} at a slightly lower energy state and V^{5+} at a slightly higher energy state, respectively.[34–36] Fittings and subsequent calculations based on peak areas revealed that the average valence states of vanadium in VO_x-NT and K-VO_x-NT are +4.38 and +4.57, respectively. In comparison with VO_x-NT, the proportion of V^{5+} in K-VO_x-NT slightly increases after K^+ exchange. This may be due to the fact that the presence of substantial dodecylamine on the surface and between the interlayers of VO_x-NT could influence the accurate survey of vanadium valence state because XPS is a surface analysis technique. Based on the XPS results of V2p in K-VO_x-NT, its vanadium valence state is very close to that in V_7O_{16} reported in previous literature.[23,25,37] So, it confirms the structural concept mentioned earlier for the VO_x layer in samples.

Fig. 6(a) and (b) depict the first three cyclic voltammetry (CV) curves for VO_x-NT and K-VO_x-NT with a scan rate of 0.2 mV s^{-1} in the voltage range of 1.5–3.8 V. For VO_x-NT, the initial cathodic scan reveals a distinct reduction peak at ~1.7 V, which is significantly different from the 2nd scan and primarily due to the formation of an irreversible solid electrolyte interface (SEI) film on the surface of the electrode during the initial discharge process.[7] This also leads to a lower initial coulombic efficiency (ICE). The 2nd and 3rd CV curves of VO_x-NT lack clear redox

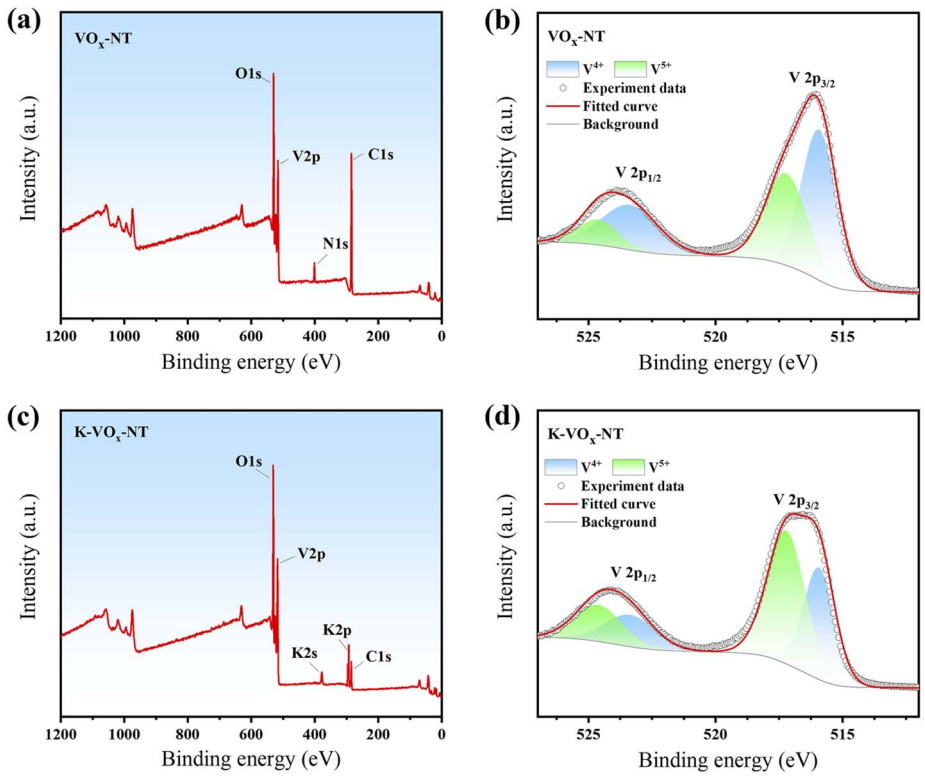

Fig. 5 XPS full (a, c) and V 2p fine (b, d) survey spectra for VO_x-NT and K-VO_x-NT.

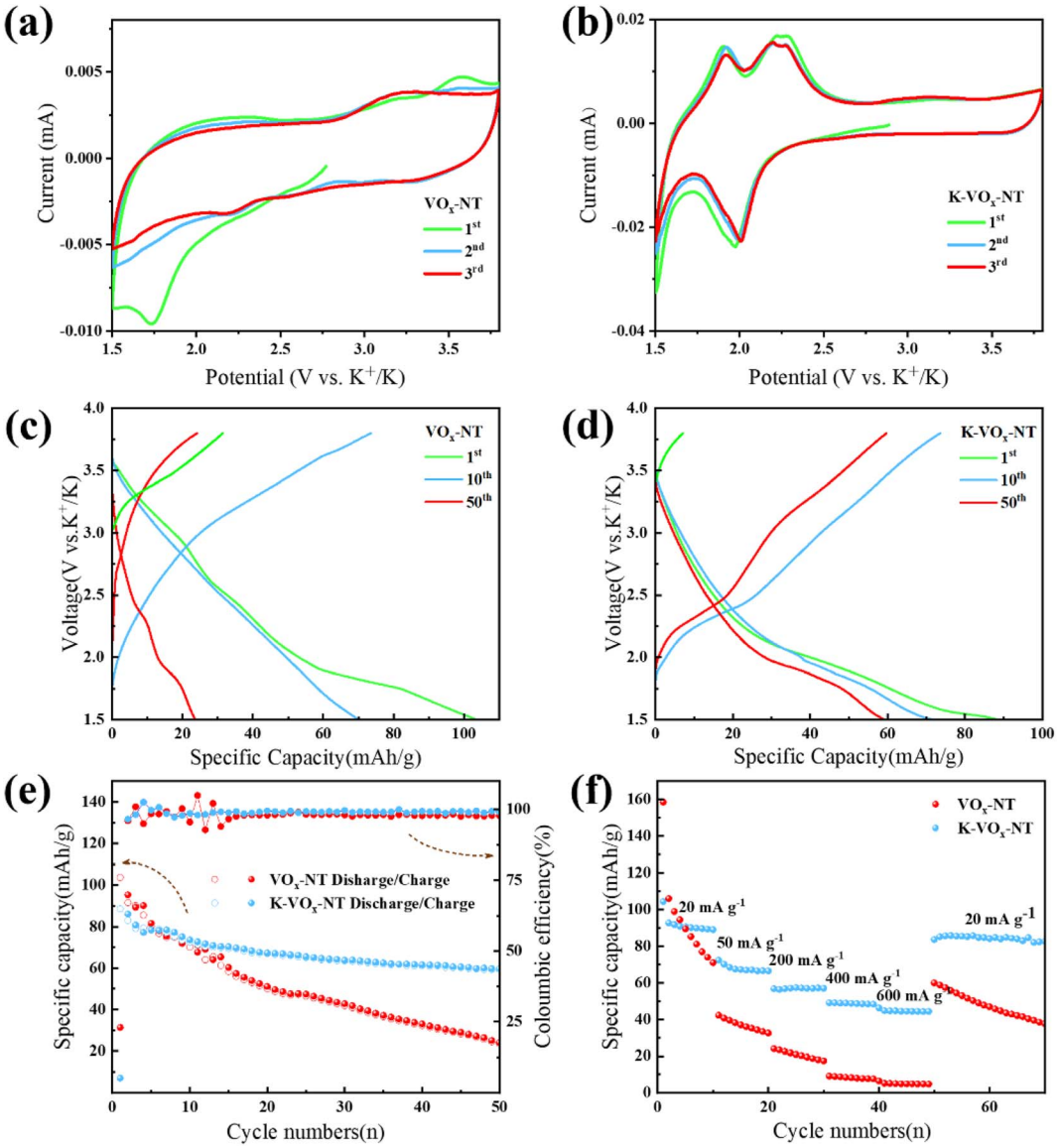

Fig. 6 Initial three CV curves of VO_x-NT (a) and K-VO_x-NT (b) at a scan rate of 0.2 mV s^{-1}; GCD profiles at the 1st, 10th and 50th cycles for VO_x-NT (c) and K-VO_x-NT (d) under 50 mA g^{-1} in the voltage region of 1.5–3.8 V; cycling performances (e) under 50 mA g^{-1} and rate capabilities (f) for VO_x-NT and K-VO_x-NT under different current densities.

peaks and show a certain degree of noncoincidence, implying its amorphous feature and subsequent poor cycling stability. By contrast, the initial cathodic scan for K-VO_x-NT reveals less deviation from 2nd and 3rd scans, indicating the formation of a less obvious SEI film and higher ICE compared to VO_x-NT. The CV curves for K-VO_x-NT overlap well and exhibit two pairs of obvious redox peaks at ~1.9/1.5 V and ~2.2/2.0 V, suggesting its good cycling stability and reversible phase transition for K^+ storage. Fig. 6(c) and (d) show the GCD profiles of the two samples at the 1st, 10th and 50th cycles. As VO_x-NT and K-VO_x-NT are initially in a charged state with insufficient K^+, their first charging curves are incomplete. Their charge capacities are mainly attributed to self-discharge and the extraction of a small amount of structural K^+. It can be observed that the specific capacity of VO_x-NT significantly decreases over cycles without distinct voltage plateaus, which is consistent with its CV results. In comparison, K-VO_x-NT maintains a high-capacity retention upon cycling with pronounced voltage plateaus, as corroborated by its CV results. To further investigate the K^+ storage mechanism of K-VO_x-NT during the discharge process, *ex situ* XRD tests at pristine and discharge to 2.0 V and 1.5 V states were performed, as illustrated in Fig. S3.† It indicates a slight contraction for the (001) plane of K-VO_x-NT, which can be attributed to the enhanced interaction between intercalated K^+ and negatively charged VO_x layers as well as the reduced electrostatic repulsion between O^{2-} in adjacent layers. Raman spectra were collected at different discharge states for K-VO_x-NT and are shown in Fig. S4(a),† which illustrates the obvious transformation of V^{5+} to V^{4+} during discharge. The V2p fine spectrum in the fully discharged state is shown in Fig. S4(b),†

which indicates that a portion of V^{4+} and V^{5+} is reduced to V^{3+} and V^{4+} upon K^+ intercalation, respectively.

Cycling performances of the two samples at 50 mA g^{-1} between 1.5 and 3.8 V are depicted in Fig. 6(e). VO_x-NT demonstrates a specific capacity of 103.7 mA h g^{-1}, 70.2 mA h g^{-1} and 23.6 mA h g^{-1} for the 1st, 10th and 50th discharges, respectively. Under the same condition, K-VO_x-NT delivers a capacity of 88.5 mA h g^{-1}, 72.5 mA h g^{-1} and 59.2 mA h g^{-1}, respectively. The result indicates that K-VO_x-NT possesses significantly better cycling stability compared with VO_x-NT, which can be attributed to the effective removal of the electrochemically inactive dodecylamine, thereby diminishing its possible side reactions with the electrode or electrolyte. Due to the introduction of the organic template during the synthesis process and the subsequent K^+ exchange step, it is challenging to accurately determine the exact stoichiometric molecular formula of VO_x-NT and K-VO_x-NT. The slight shift observed in the (001) peak of the XRD pattern for discharged K-VO_x-NT suggests the intercalation of K^+ into the VO_x layers of K-VO_x-NT. The qualitative charge–discharge reactions of VO_x-NT and K-VO_x-NT can be described by the following equations:

$$VO_x\text{-NT} + yK^+ + ye^- \leftrightarrow K_yVO_x\text{-NT} \quad (1)$$

$$K\text{-}VO_x\text{-NT} + zK^+ + ze^- \leftrightarrow K_{1+z}VO_x\text{-NT} \quad (2)$$

At the beginning of the reversible potassium storage stage, $y > z$. However, as cycling progresses, $z > y$. Rate performances of the two samples at different current densities are presented in Fig. 6(f). VO_x-NT displays a specific capacity of 71.0, 32.5, 17.4, 6.4, 4.7 and 46.8 mA h g^{-1} under 20, 50, 200, 400, 600 and 20 mA g^{-1} for the 10th discharge, respectively. Under the same conditions, the corresponding capacity values for K-VO_x-NT are 89.0, 66.4, 56.9, 46.2, 44.3 and 84.1 mA h g^{-1}, respectively. This indicates that K-VO_x-NT, which profits from the effective removal of dodecylamine without electrochemical activity and meanwhile maintains its nanotubular structure, can exhibit significantly improved cycling and rate performance compared to pristine VO_x-NT.

Fig. 7 gives the TEM images of VO_x-NT (a, b) and K-VO_x-NT (c, d) after 100 cycles at 50 mA h g^{-1}. It can be observed that the hollow nanotubular structure of VO_x-NT collapses severely, whereas K-VO_x-NT retains its hollow nanotubular morphology well. This indicates that the good microstructure retention of K-VO_x-NT can be responsible for its better cycling performance compared to VO_x-NT.

Nyquist plots (dot), relevant fitting results (line) and equivalent circuit (inset) of VO_x-NT and K-VO_x-NT at the open circuit voltage (OCV), 3rd cycle and 100th cycle are presented in Fig. 8(a) and (b), respectively. Nyquist plots are characterized by a semicircle in the middle and high frequency regions associated with charge transfer resistance (R_{ct}) and a sloping line in the low frequency region related to Warburg impedance (W_o). R_{ct} indicates the difficulty of K^+ passing through the electrolyte/electrode interface, while W_o reflects the diffusion impedance of K^+ within the electrode.[38] Additionally, the intercept of the Nyquist plot with the real impedance (Z') axis represents the electrolyte resistance (R_e). The constant phase element (CPE) in the equivalent circuit stands for the capacitive behavior related to charge transfer at the electrolyte/electrode interface.[39]

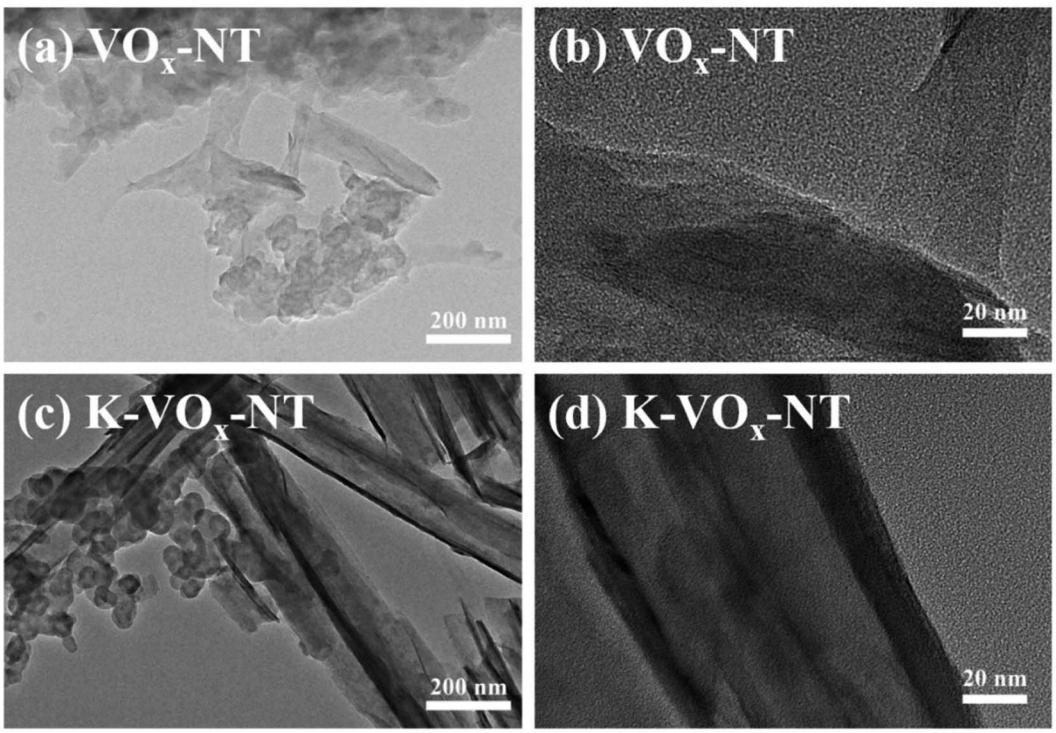

Fig. 7 TEM images of VO_x-NT (a, b) and K-VO_x-NT (c, d) at different magnifications after 100 cycles.

Through fitting based on the equivalent circuit, the R_{ct} values of VO_x-NT at the OCV, 3rd and 100th cycles were 12 190 Ω, 17 286 Ω and 21 520 Ω, respectively. By contrast, the R_{ct} values of K-VO_x-NT at the corresponding states were 11 230 Ω, 16 440 Ω and 13 990 Ω, respectively. It is evident that the R_{ct} value of VO_x-NT increased with cycling, which correlates with its microstructural degradation upon repeated K^+ insertion/extraction. Conversely, the R_{ct} value of K-VO_x-NT initially increased, but showed a descending trend as the cycling continued. On one hand, it is related to the good microstructural preservation of K-VO_x-NT upon cycling. On the other hand, it may benefit from the gradual maturation of the SEI film on the surface of K-VO_x-NT during cycling, facilitating K^+ migration between the electrolyte and electrode. EIS tests indicate that the effective removal of dodecylamine intercalated in VO_x-NT will be conducive to dynamic behavior of K^+ at the electrode/electrolyte interface, maintaining lower R_{ct}.

GITT tests were conducted to explore the K^+ diffusion and transport properties in VO_x-NT and K-VO_x-NT, acquiring their K^+ diffusion coefficients (D_{K^+}). GITT curves and log(D_{K^+}) *vs.* working potential for the two samples during charge/discharge processes are illustrated in Fig. 8(c) and (d). Their representative titration curves in a single pulse charge and relaxation are depicted in Fig. 8(e) and (f). Here, τ represents the pulse time, ΔE_S denotes the change of steady-state voltage before and after pulse stimulation and ΔE_τ denotes the real-time potential variation under pulse stimulation. Based on formula (3), D_{K^+} for the two samples can be calculated.[30,39]

$$D_{K^+} = \frac{4}{\pi\tau}\left(\frac{m_B V_m}{M_B S}\right)^2\left(\frac{\Delta E_S}{\Delta E_\tau}\right)^2 \quad (3)$$

where m_A, V_M and M_A denote the mass, molar volume and molar mass of the target active cathode, respectively. S refers to the geometric area of the target cathode slice.[21,40] The results

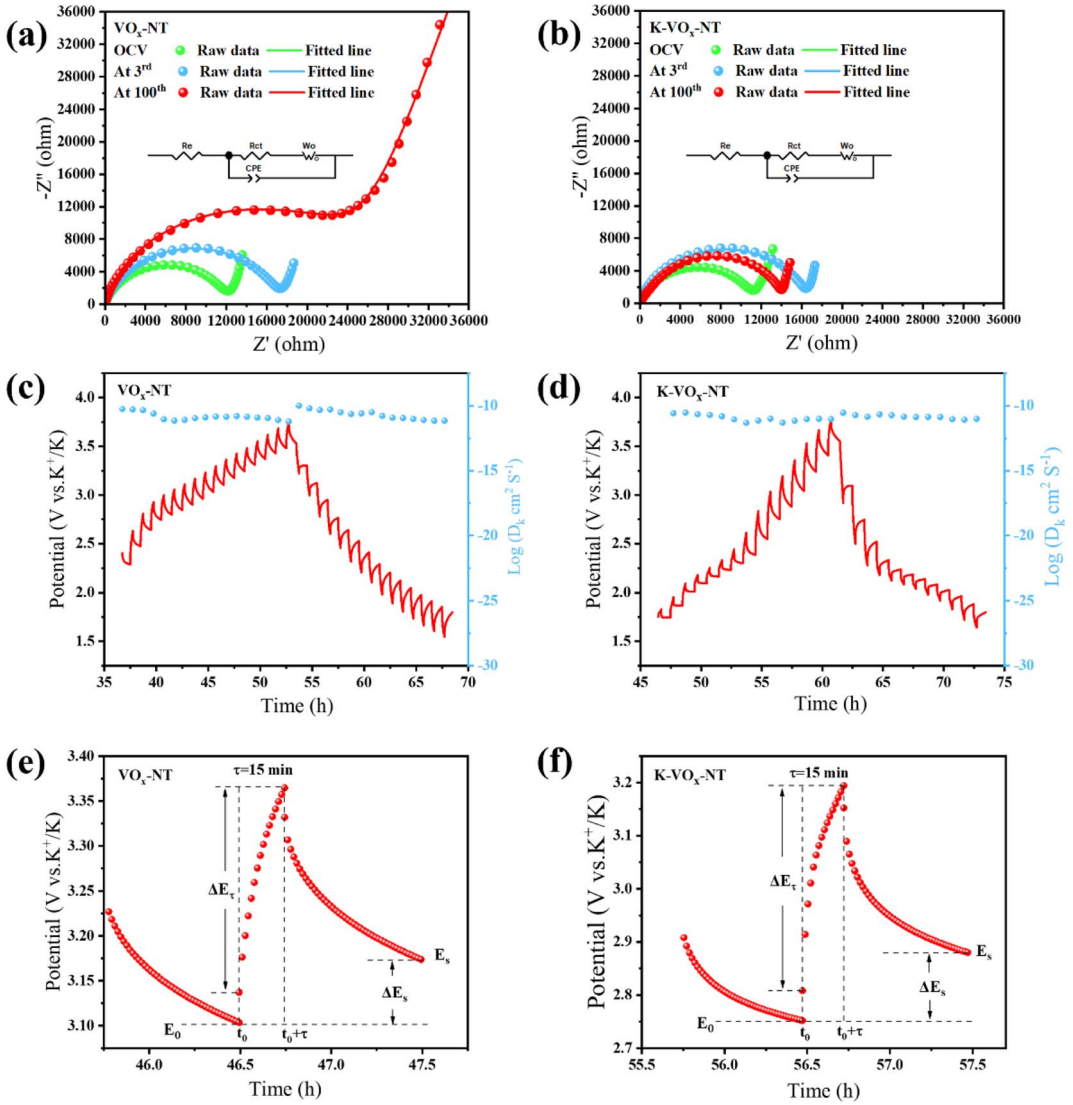

Fig. 8 Nyquist plots of VO_x-NT (a) and K-VO_x-NT (b) from EIS tests at OCV and the 1st and 100th cycles; potential response curves during GITT measurements and the corresponding logarithm of K^+ diffusion coefficients (D_{K^+}) for VO_x-NT (c) and K-VO_x-NT (d); representative processes (e and f) of single pulse and relaxation during GITT measurements for the two samples.

display that D_{K^+} for VO_x-NT is distributed between 6.26×10^{-12} and 6.41×10^{-11} cm^2 s^{-1}, with an average value of $\sim 2.45 \times 10^{-11}$ cm^2 s^{-1}. As regards K-VO_x-NT, its D_{K^+} is in the range of 4.94×10^{-12} to 2.91×10^{-11} cm^2 s^{-1}, with an average value of $\sim 1.02 \times 10^{-11}$ cm^2 s^{-1}. It can be seen that the average D_{K^+} value for K-VO_x-NT is on the same order of magnitude as that of VO_x-NT, but slightly lower compared to that of VO_x-NT. It may be due to the noticeably reduced interlayer spacing in K-VO_x-NT *via* K^+ exchange, which suggests that a wider interlayer spacing between VO_x layers facilitates the transport of K^+ with a large radius at the beginning. This is also associated with the initial higher K^+ storage capacity of VO_x-NT. Notably, the D_{K^+} values for VO_x-NT and K-VO_x-NT in our study have a distinct advantage when compared to other layered vanadium-based cathodes reported in the literature, possibly benefitting from the wider interlayer spacing between VO_x layers.[21,30,41]

Fig. 9(a)–(c) give the typical CV curves for VO_x-NT and K-VO_x-NT at different scan rates from 0.2 to 2.0 mV s^{-1} between 1.5 and 3.8 V, respectively. Notably, K-VO_x-NT exhibits obvious redox peaks, whereas those for VO_x-NT are less pronounced, indicating that K-VO_x-NT maintains good reversible K^+ intercalation and deintercalation characteristics even under rapid scanning. The relationship between the peak current (i) of CV scan and scanning rate (v) is described by the following equations:[39,42,43]

$$i = av^b \quad (4)$$

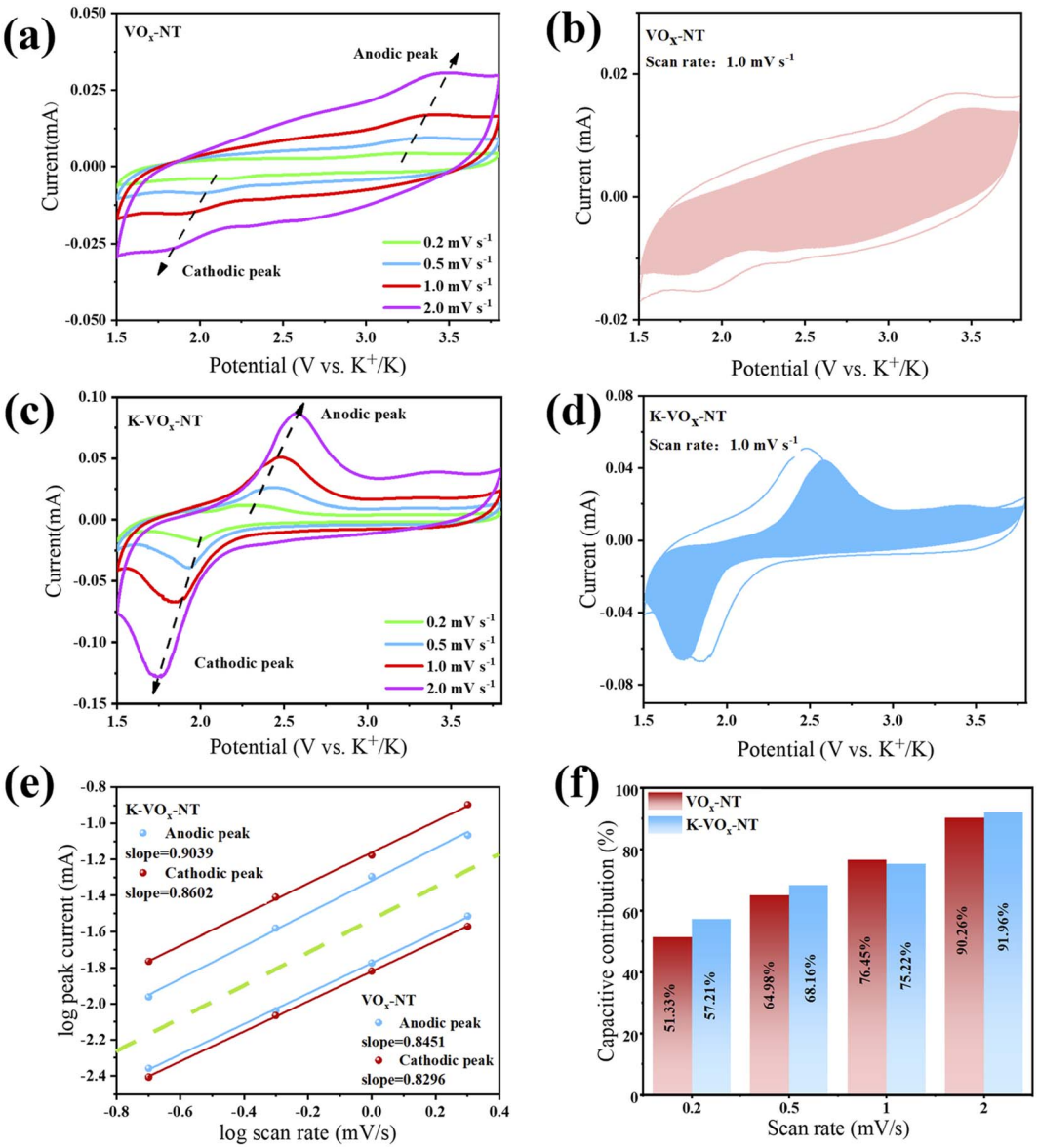

Fig. 9 Typical CV curves (a–c) at different scanning rates (v) and linear fitting relationship (e) between log(i) *vs.* log(v) for VO_x-NT and K-VO_x-NT (i is the current value of the anodic or cathodic peak); pseudocapacitive contributions (shaded areas) from the surface-induced process in a representative CV test at 1.0 mV s^{-1} for VO_x-NT (b) and K-VO_x-NT (d); histogram (f) displaying the proportions of pseudocapacitance at increasing scan speeds for the two samples.

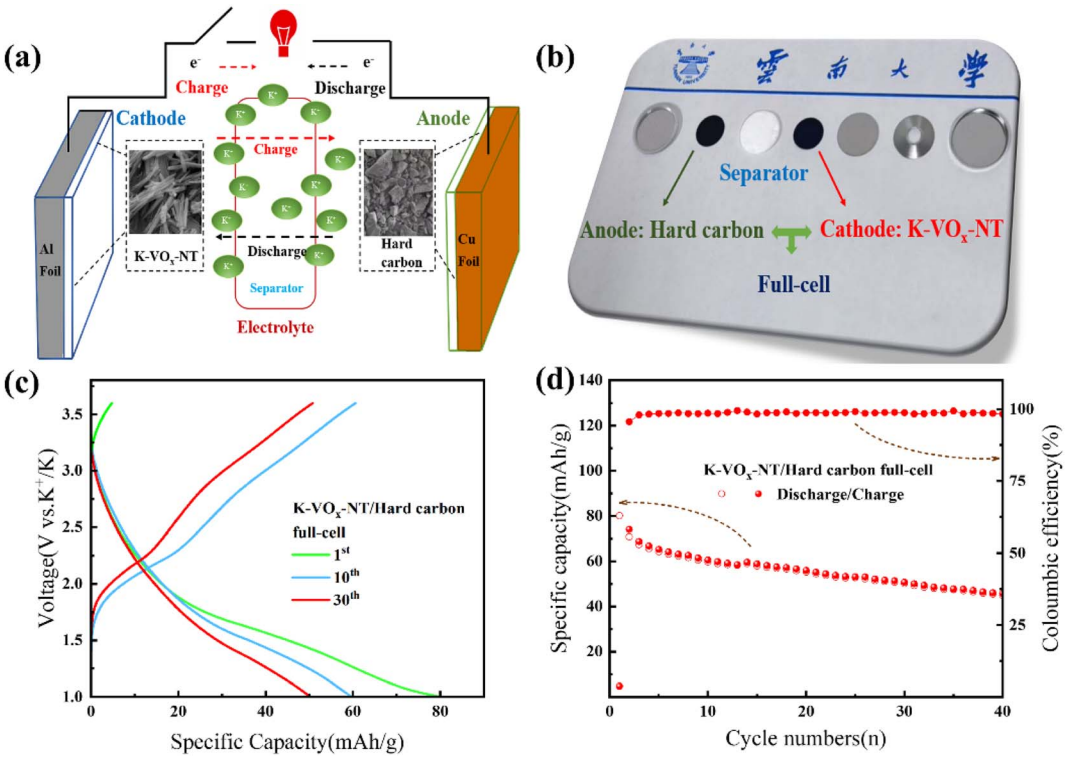

Fig. 10 Schematic of the full-cell configuration (a) and actual structure for the coin-prototype cell (b) in laboratory; the initial three GCD profiles (c) and cycling performance (d) of the full-cell (N/P ratio: ~1.1) using K-VO_x-NT as the cathode and hard carbon as the anode under 50 mA g^{-1} between 1.0 and 3.6 V.

$$\log(i) = \log(av^b) = \log(a) + b\log(v) \quad (5)$$

By fitting the logarithmic relationship between anodic/cathodic peak currents (i) and scan rates (v), we obtain a linear correlation. The slope is the b value in eqn (4), which provides insights into the K^+ storage mechanism within the electrode. Specifically, when b is close to 0.5, it indicates that the storage of K^+ is predominantly controlled by internal diffusion. If the b value approaches 1, it suggests that surface pseudocapacitive behavior dominates the K^+ storage.[41,42] The fitting results of b values for VO_x-NT and K-VO_x-NT are depicted in Fig. 9(e), whose average values are ~0.84 and 0.88, respectively. It indicates that K^+ storage contributions for both samples are predominantly governed by surface pseudocapacitive behavior. Among them, K-VO_x-NT demonstrates a slightly stronger pseudocapacitive contribution compared to VO_x-NT.

To quantitatively describe the K^+ storage contributions of the two samples, we divided the total current at specific voltages into surface-controlled and diffusion-controlled sections by the following formulas:[28,41,43]

$$i(V) = k_1 v + k_2 v^{1/2} \quad (6)$$

$$\frac{i(V)}{v^{1/2}} = k_1 v^{1/2} + k_2 \quad (7)$$

Herein, v represents the scan rate, while k_1 and k_2 are constants. $k_1 v$ stands for the surface-controlled (pseudocapacitive) contribution and $k_2 v^{1/2}$ the diffusion-controlled contribution. By fitting the linear relationship between $i/v^{1/2}$ and $v^{1/2}$ at specific voltages, a series of k_1 and k_2 values dependent on voltage can be obtained. It allows us to visually distinguish different contributions to K^+ storage capacity through the area ratio in a closed CV curve at different scan rates. Fig. 9(b) and(d) depict the pseudocapacitive contributions (shaded areas) of VO_x-NT and K-VO_x-NT at a typical scan rate of 1.0 mV s^{-1}, respectively. Their corresponding proportions are 76.45% and 75.22%, respectively. Through the same analytical method, the pseudocapacitive contributions for the two samples under 0.2 to 2 mV s^{-1} are illustrated in Fig. 9(f) (detailed results are provided in Fig. S5†). It can be concluded that the ratio of pseudocapacitive contributions will enhance as the scan rate increases. In general, K-VO_x-NT displays a slightly higher pseudocapacitive contribution in comparison with VO_x-NT.

To evaluate the K^+ storage performance of the K-VO_x-NT cathode in practical applications, we assembled a full-cell using hard carbon as the anode. While standard anode materials for lithium-ion and sodium-ion batteries are well-established, a widely accepted anode for PIBs remains lacking. Hard carbon, which is known for its excellent potassium storage performance and low cost, is considered a promising anode material for PIBs.[44] The details for the electrochemical performance of hard carbon in a half-cell configuration are illustrated in Fig. S6.† The configuration of the full-cell and actual structure of the coin-prototype cell in our laboratory are illustrated in Fig. 10(a) and (b), respectively. Fig. 10(c) and (d) present the

initial three GCD profiles and cycling performance of the K-VO_x-NT/Hard carbon full-cell with a N/P ratio of ~1.1. The specific capacity of the full-cell was determined based on the mass of the active K-VO_x-NT cathode. The results showed that this full-cell delivered an initial discharge specific capacity of 80.1 mA h g^{-1} at 50 mA g^{-1} between 1.0 and 3.6 V. For the 10th and 30th cycles, its discharge specific capacities decreased to 59.8 and 50.2 mA h g^{-1}, respectively. The energy density of the full-cell is illustrated in Fig. S7.† For the evaluation of rate capability of the full-cell, we employed different N/P ratios of ~1.1 and 4.0 (refer to Fig. S8†). It was observed that a higher N/P ratio (~4.0) enables the K-VO_x-NT cathode to fully demonstrate its ideal rate capability for K^+ storage. This can be primarily attributed to the fact that, at the condition of high N/P ratio, the hard carbon anode mainly operates by capacitive behavior for K^+ storage, thereby minimizing the polarization effects on the full-cell, as discussed in the ESI.†

4 Conclusion

In this study, a novel K-VO_x-NT cathode with a hollow and multi-walled structure has been successfully fabricated by a soft template technique under hydrothermal conditions combined with a subsequent K^+ exchange process. Systematic characterization confirmed that the dodecylamine intercalated between vanadium oxide layers, which lacks potassium storage activity, was effectively removed after K^+ exchange, while the special hollow and multi-walled structure of VO_x-NT was well preserved. K-VO_x-NT as the cathode for PIBs exhibited a superior capacity retention (74.4%) after 50 cycles under a current density of 50 mA g^{-1} compared to VO_x-NT (merely 17.9%) without the exchange of K^+ under identical conditions. Besides, K-VO_x-NT displayed significantly enhanced rate capability and lower charge transfer resistance compared with VO_x-NT. This is attributed to the effective removal of the organic dodecylamine template without electrochemical activity in VO_x-NT. On the other hand, K-VO_x-NT maintained its special hollow and multi-walled nanotubular microstructure after K^+ exchange, which can provide abundant active sites during repeated K^+ insertion/extraction processes. The potassium storage performance test indicated that the capacitive contribution predominantly governs the potassiation/depotassiation processes for K-VO_x-NT. Furthermore, the potassiation process in K-VO_x-NT was accompanied by the valence state transition of vanadium from V^{5+} to V^{3+}. This K-VO_x-NT could be adopted as a promising cathode candidate for application in PIBs. Moreover, the practical performance of the K-VO_x-NT full-cell was evaluated using hard carbon as the anode, providing a comprehensive assessment of its application potential. Our research provides valuable guidance for further exploration of vanadium-based cathodes used in PIBs.

Data availability

The fundamental data are within the manuscript and its "ESI†" file. Other relevant data are available from the authors upon reasonable request.

Author contributions

Yuan Xie: conceptualization, investigation, methodology, writing – original draft. Jia Wen: conceptualization; software. Junyuan Huang: investigation, visualization. Rong Jiang: visualization. Longjun Dai: formal analysis, software. Yang Ren: validation. Zhu Liu: methodology, data curation. Xiaowei Zhou: supervision, data curation, funding acquisition, writing – review & editing.

Conflicts of interest

The authors declare that they have no competing financial interest.

Acknowledgements

It is very grateful to financial supports from the National Natural Science Foundation of China (Grant No. 12264054, 12464016), General & Key Project of Applied Basic Research of Yunnan Science and Technology Department (Grant No. 202301AT070139, 202401AS070130), Double First Class Joint Special Key Project of Yunnan Science and Technology Department & Yunnan University (Grant No. 202401BF070001-012), Xingdian Talent Support Program for Youth Project, Postgraduate Quality Course (Nanomaterials and Nanotechnology) Construction Project of Yunnan Province in 2024 and Postgraduate Research Innovation Project of Yunnan University (Grant No. KC-23235277, KC-23235538).

References

1 J. Li, J. Fleetwood, W. B. Hawley, *et al.*, From materials to cell: state-of-the-art and prospective technologies for lithium-ion battery electrode processing, *Chem. Rev.*, 2021, **122**(1), 903–956.
2 L. Niu, R. Zhang, Q. Zhang, *et al.*, Carbon-coated silicon/graphite oxide composites as anode materials for highly stable lithium-ion batteries, *Phys. Chem. Chem. Phys.*, 2024, **26**, 17292–17302.
3 Y. Tong, Y. Wu, Z. Liu, *et al.*, Fabricating multi-porous carbon anode with remarkable initial coulombic efficiency and enhanced rate capability for sodium-ion batteries, *Chin. Chem. Lett.*, 2023, **34**, 107443.
4 Y. Wang, L. Xie, R. Huang, *et al.*, Theoretical investigation of Janus Ti_2BST (T = O, Se) monolayers as anode materials for Na/K-ion batteries, *Phys. Chem. Chem. Phys.*, 2024, **26**, 18394–18401.
5 Z. Chen, H. Lin, Y. Tan, *et al.*, Anchoring multi-coordinated bismuth metal atom sites on honeycomb-like carbon rods achieving advanced potassium storage, *Adv. Funct. Mater.*, 2024, 2407653.
6 Z. Chen, Y. Wu, X. Liu, *et al.*, Bi/Bi_3Se_4 nanoparticles embedded in hollow porous carbon nanorod: High rate capability material for potassium-ion batteries, *J. Energy Chem.*, 2023, **81**, 462–471.

7 Y. Tan, H. Lin, Z. Chen, *et al.*, Regulating the coordination microenvironment of atomic bismuth sites in nitrogen-rich carbon nanosheets as anode for superior potassium-ion batteries, *J. Energy Chem.*, 2024, **99**, 365–374.
8 N. Cheng, P. Xu, B. Lu, *et al.*, Covalent sulfur as stable anode for potassium ion battery, *J. Energy Chem.*, 2021, **62**, 645–652.
9 J. Zhang, T. Liu, X. Cheng, *et al.*, Development status and future prospect of non-aqueous potassium ion batteries for large scale energy storage, *Nano Energy*, 2019, **60**, 340–361.
10 L. Wu, H. Fu, S. Li, *et al.*, Phase-engineered cathode for super-stable potassium storage, *Nat. Commun.*, 2023, **14**(1), 644.
11 Y. Zhang, Y. Wang, L. Hou, *et al.*, Recent Progress of Carbon-Based Anode Materials for Potassium Ion Batteries, *Chem. Rec.*, 2022, **22**(10), e202200072.
12 X. Liu, Z. Sun, Y. Sun, *et al.*, Fast and long-lasting potassium-ion storage enabled by rationally engineering strain-relaxation Bi/Bi_2O_3 nanodots embedded in carbon sheets, *Adv. Funct. Mater.*, 2023, 2307205.
13 Y. Lee, J. K. Yoo, H. Park, *et al.*, An exceptionally large energy cathode with the K–SO 4–Cu conversion reaction for potassium rechargeable batteries, *J. Mater. Chem. A*, 2021, **9**(9), 5475–5484.
14 B. Tian, W. Tang, C. Su, *et al.*, Reticular V_2O_5 0.6 H_2O xerogel as cathode for rechargeable potassium ion batteries, *ACS Appl. Mater. Interfaces*, 2018, **10**(1), 642–650.
15 L. Li, Z. Hu, Y. Lu, *et al.*, A Low-strain potassium-rich prussian blue analogue cathode for high power potassium-ion batteries, *Angew. Chem., Int. Ed.*, 2021, **133**(23), 13160–13166.
16 C. Gao, Y. Lei, Y. Wei, *et al.*, Coexistence of two coordinated states contributing to high-voltage and long-life Prussian blue cathode for potassium ion battery, *Chem. Eng. J.*, 2022, **431**, 133926.
17 S. Liu, L. Kang and S. C. Jun, Challenges and strategies toward cathode materials for rechargeable potassium-ion batteries, *Adv. Mater.*, 2021, **33**(47), 2004689.
18 Y. S. Xu, S. Y. Duan, Y. G. Sun, *et al.*, Recent developments in electrode materials for potassium-ion batteries, *J. Mater. Chem. A*, 2019, **7**(9), 4334–4352.
19 W. Li, Z. Bi, W. Zhang, *et al.*, Advanced cathodes for potassium-ion batteries with layered transition metal oxides: a review, *J. Mater. Chem. A*, 2021, **9**(13), 8221–8247.
20 X. Xu, F. Xiong, J. Meng, *et al.*, Vanadium-based nanomaterials: a promising family for emerging metal-ion batteries, *Adv. Funct. Mater.*, 2020, **30**(10), 1904398.
21 L. Deng, X. Niu, G. Ma, *et al.*, Layered potassium vanadate $K_{0.5}V_2O_5$ as a cathode material for nonaqueous potassium ion batteries, *Adv. Funct. Mater.*, 2018, **28**(49), 1800670.
22 Y. Xu, H. Dong, M. Zhou, *et al.*, Ammonium vanadium bronze as a potassium-ion battery cathode with high rate capability and cyclability, *Small Methods*, 2019, **3**(8), 1800349.
23 V. Petkov, P. Y. Zavalij, S. Lutta, *et al.*, Structure beyond Bragg: Study of V_2O_5 nanotubes, *Phys. Rev. B*, 2004, **69**(8), 085410.
24 S. Nordlinder, K. Edström and T. Gustafsson, The performance of vanadium oxide nanorolls as cathode material in a rechargeable lithium battery, *Electrochem. Solid-State Lett.*, 2001, **4**, A129.
25 C. K. Christensen, E. D. Bøjesen, D. R. Sørensen, *et al.*, Structural evolution during lithium-and magnesium-ion intercalation in vanadium oxide nanotube electrodes for battery applications, *ACS Appl. Nano Mater.*, 2018, **1**(9), 5071–5082.
26 J. Wei, Y. Zhu and J. Zhang, Effects of synthetic conditions on the structure and morphology of open-ended vanadium oxide nanotubes and study of their growth mechanism, *Chin. Sci. Bull.*, 2007, **52**, 1920–1924.
27 R. H. Kim, J. S. Kim, H. J. Kim, *et al.*, Highly reduced VO_x nanotube cathode materials with ultra-high capacity for magnesium ion batteries, *J. Mater. Chem. A*, 2014, **2**(48), 20636–20641.
28 Q. Zong, Q. Q. Wang, C. Liu, *et al.*, Potassium ammonium vanadate with rich oxygen vacancies for fast and highly stable Zn-ion storage, *ACS Nano*, 2022, **16**(3), 4588–4598.
29 Z. Feng, J. Sun, Y. Liu, *et al.*, Polypyrrole-intercalation tuning lamellar structure of $V_2O_5 \cdot nH_2O$ boosts fast zinc-ion kinetics for aqueous zinc-ion battery, *J. Power Sources*, 2022, **536**, 231489.
30 X. Niu, J. Qu, Y. Hong, *et al.*, High-performance layered potassium vanadium oxide for K-ion batteries enabled by reduced long-range structural order, *J. Mater. Chem. A*, 2021, **9**(22), 13125–13134.
31 E. A. Esparcia, M. S. Chae, J. D. Ocon, *et al.*, Ammonium vanadium bronze ($NH_4V_4O_{10}$) as a high-capacity cathode material for nonaqueous magnesium-ion batteries, *Chem. Mater.*, 2018, **30**(11), 3690–3696.
32 H. Yang, Q. Li, L. Sun, *et al.*, MXene-Derived Na^+-Pillared Vanadate Cathodes for Dendrite-Free Potassium Metal Batteries, *Small*, 2024, **20**(5), 2306572.
33 H. Zhou H, X. Yan, L. Ding, *et al.*, Ultra-stable aqueous nickel-ion storage achieved by iron-ion pre-introduction assisted hydrated vanadium oxide cathode, *Energy Storage Mater.*, 2024, **68**, 103340.
34 W. Chen, L. Mai, J. Peng, *et al.*, Raman spectroscopic study of vanadium oxide nanotubes, *J. Solid State Chem.*, 2004, **177**(1), 377–379.
35 A. Wang, D. H. Liu, L. Yang, *et al.*, Building stabilized $Cu_{0.17}Mn_{0.03}V_2O_5$– 2.16 H_2O cathode enables an outstanding room-/low-temperature aqueous Zn-ion batteries, *Carbon Energy*, 2024, e512.
36 H. He, K. Cao, S. Zeng, *et al.*, $K_2VOP_2O_7$ as a novel high-voltage cathode material for potassium ion batteries, *J. Power Sources*, 2023, **587**, 233715.
37 F. Yang, Y. Zhu, Y. Xia, *et al.*, Fast Zn^{2+} kinetics of vanadium oxide nanotubes in high-performance rechargeable zinc-ion batteries, *J. Power Sources*, 2020, **451**, 227767.
38 K. Yang, J. Tang, Y. Liu, *et al.*, Controllable synthesis of peapod-like Sb@C and corn-like C@Sb nanotubes for sodium storage, *ACS Nano*, 2020, **14**(5), 5728–5737.
39 C. Chen, Q. Deng, Q. Zhang, *et al.*, PEDOT-intercalated $NH_4V_3O_8$ nanobelts as high-performance cathode materials

for potassium ion batteries, *J. Colloid Interface Sci.*, 2023, **633**, 619–627.

40 J. Kim, S. H. Lee, C. Park, *et al.*, Controlling vanadate nanofiber interlayer *via* intercalation with conducting polymers: cathode material design for rechargeable aqueous zinc ion batteries, *Adv. Funct. Mater.*, 2021, **31**(26), 2100005.

41 Y. Zhang, X. Niu, L. Tan, *et al.*, $K_{0.83}V_2O_5$: a new layered compound as a stable cathode material for potassium-ion batteries, *ACS Appl. Mater. Interfaces*, 2020, **12**(8), 9332–9340.

42 Y. Qi, M. Liao, Y. Xie, *et al.*, Long-life vanadium oxide cathode for zinc battery enabled by polypyrrole intercalation and concentrated electrolyte, *Chem. Eng. J.*, 2023, **470**, 143971.

43 G. Xu, X. Liu, S. Huang, *et al.*, Freestanding, Hierarchical, and Porous Bilayered $Na_xV_2O_5 \cdot nH_2O$/rGO/CNT Composites as High-Performance Cathode Materials for Nonaqueous K-Ion Batteries and Aqueous Zinc-Ion Batteries, *ACS Appl. Mater. Interfaces*, 2019, **12**(1), 706–716.

44 S. Alvin, H. S. Cahyadi, J. Hwang, *et al.*, Revealing the intercalation mechanisms of lithium, sodium, and potassium in hard carbon, *Adv. Energy Mater.*, 2020, **10**(20), 2000283.